Reverse design of pixel-type terahertz band-pass filters

XUEWEI JU,[1,3] GUOFENG ZHU,[1,3] FENG HUANG,[1,4] ZHENRONG DAI,[1] YANQING CHEN,[1] CUIXIA GUO,[1] LI DENG,[2] AND XIANGFENG WANG[1,5] 🆔

[1]*School of Mechanical Engineering and Automation, Fuzhou University, Fuzhou, 350108, China*
[2]*School of Physics & Electronic Science, East China Normal University, Shanghai, 200241, China*
[3]*Equal contributors*
[4]*huangf@fzu.edu.cn*
[5]*xfwang@fzu.edu.cn*

Abstract: Reverse design is a frontier direction in the optical research field. In this work, reverse design is applied to the design of terahertz devices. We have employed direct binary search (DBS) and binary particle swarm optimization (BPSO) algorithms to design pixel-type terahertz band-pass filters, respectively. Through a comparative analysis of the designed devices, we found that BPSO algorithm converged faster than DBS algorithm, and the device performance is better on out-of-band suppression. We have fabricated a sample utilizing femtosecond laser micromachining and characterized it by terahertz time-domain spectroscopy. The experimental results were consistent with the finite difference time domain (FDTD) simulation. Our method can simultaneously optimize multiple characteristics of the band-pass filters, including the peak transmittance, out-of-band transmittance, bandwidth, and polarization stability, which can not be achieved by traditional optical design methods.

1. Introduction

Terahertz (THz) band-pass filters (BPFs), a type of functional devices that passes frequencies within a certain range and rejects/attenuates frequencies outside that range, are widely applied in THz communication, imaging, stealth and other fields [1,2]. There are many approaches to fabricate THz BPFs, including fully enclosed metal waveguides [3], photonic crystals [4], frequency selective surfaces [5,6], and metamaterials [7], etc. Traditional design methods excessively rely on the designer's experience and optical theories, by continually adjusting the structural parameters of the devices to achieve particular performance, such as THz filters [8], demultiplexers [9], polarizers [10], and power splitters [11]. Miniaturized, integrated and high-performance THz functional devices are highly desired.

Reverse design method (RDM) is a unique tactic that, by treating target performance as evaluation standards, uses intelligent algorithms to optimize the initial structure, and ultimately finds a satisfactory device. The novel approach, different from the traditional method, accomplish the design by exploring all possible structures in the whole design area, and the final achievement can be capable of more complex functions, higher performance and smaller volume [12,13]. In recent years, RDM has been widely utilized in the design of optical devices, such as a polarization beam splitter designed by direct binary search (DBS) algorithm [14], a nanophotonic wavelength router designed by genetic algorithm [15], an on-chip multi-channel focusing wavelength demultiplexer designed by objective-first algorithm [16], and so on. However, RDM has not been widely applied to the design of the THz devices.

In this work, we apply RDM to the design of THz BPFs based on two intelligent algorithms. A sample based on a simplified DBS design is prepared by femtosecond laser micromachining. The results of THz time-domain spectroscopy (TDS) measurement are highly consistent with

the finite difference time domain (FDTD) simulation results, which proves the feasibility of the method. The RDM does not need any known structure or shape, only needs to specify the design area and iterative parameters, which can realize the reverse design from performance to target structure, and provides solutions for some THz devices that are difficult to be designed by traditional methods and theories.

2.   Reverse design methods

Traditional forward design method is generally based on the specific analytical theory. For example, in order to design a THz demultiplexer based on a photonic crystal structure, a plane wave expansion method is first used to calculate its dispersion curve, and then the propagation constant can be extracted from the curve and was introduced into the self-imaging conditions to calculate the self-imaging positions [17]. Finally, the required devices can be achieved according to the self-imaging positions. The method is not only time-consuming and laborious, but also requires rich experience in theoretical analysis. It will be severely challenged when the applications of the devices are expanded to the broadband, nonlinear phenomena and integrated systems. Especially in the process of nonlinear device optimization, several interdependent characteristic parameters need to be optimized at the same time, for which the personal experience is highly crucial. However, RDM, viewing the functional parameters of the device as the evaluation indexes, utilized intelligent algorithms to find out the optimal structures. Non-periodic topological device structures can be obtained by searching the entire design space based on the algorithms, achieving complex functions and higher performance that could not be realized before. The performance of the filter is usually evaluated by the following four aspects, including peak transmittance, out-of-band suppression, passband width, and polarization stability.

2.1.   DBS algorithm

DBS is essentially a traversal search algorithm. The optimal hologram is obtained by searching the whole design area iteratively. DBS algorithm needs to recalculate the objective function when one pixel of an image is modified each time, where the image has $M \times N$ pixels. The objective function needs to be calculated for $M \times N$ times in each iteration, Thus, DBS algorithm has a large amount of calculations and is not suitable for large-area holograms.

The DBS algorithm has been applied to the design of a polarization beam splitter recently [12]. The idea can also be used for the reverse design of THz BPFs, in which we use the algorithm to optimize the unit structure of traditional frequency selective surface (FSS) [5]. The unit structure of FSS is the smallest element of two-dimensional periodical structure. A traditional cross-type FSS which works as a THz band-pass filter is shown in Fig. 1(a). The specific steps of DBS are listed below:
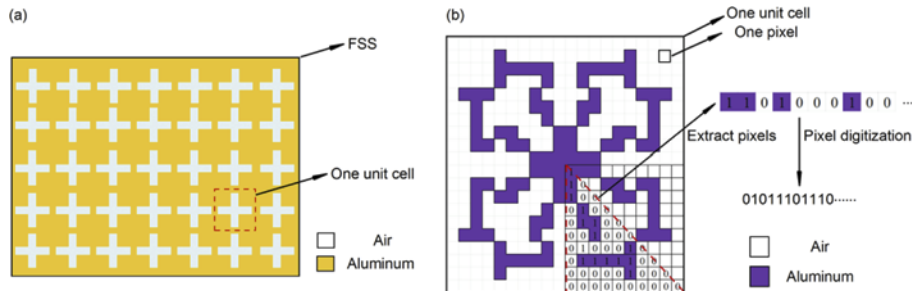
Fig. 1. (a) A traditional cross-type FSS; (b) Schematic diagram of the pixel distribution and 1/8 symmetrical unit structure surrounded by red triangle in a pixel-type THz BPF.

Step 1: The unit of FSS is divided into $M \times N$ small blocks (pixels). $M \times N$ pixels are composed of metal or air blocks representing 1 or 0, respectively. Air blocks can be removed in the device fabrication. A unit structure with $M \times N$ pixels is generated with randomly distributed 0 and 1 blocks.

Step 2: Set the objective function, also called the figure of merit (FOM), which defines the performance of the device. In the case of THz BPFs, it is the sum of the squares of the difference between the actual transmittance and the target transmittance at multiple frequencies. Then, the initial structure is imported into electromagnetic field simulation software (FDTD Solutions, Lumerical Solutions, Inc.), and the simulation results are returned and the initial FOM value is calculated.

Step 3: Randomly select one of the $M \times N$ pixels and change its state ($0 \rightarrow 1$ or $1 \rightarrow 0$). For the new structure, run an FDTD simulation, calculate its FOM value and compare it to the previous FOM value. If the FOM value is improved, keep the change. Otherwise, restore the previous value. A total of $M \times N$ changes are required, that is, traversing all pixels. It is called an iteration, and the optimal FOM value in this iteration is retained.

Step 4: Repeat **Step 3** and compare the FOM value of the last iteration with that of this iteration. If the FOM value is improved, continue to repeat **Step 3**. After a certain number of iterations, the optimization ends and the final optimized structure is output.

The objective function of THz BPFs can be defined according to its target performance, including the transmittance at the central frequency in the passband, the transmittance at FWHM, bandwidth, and the transmittance in the off-band. The FOM of THz BPFs can be expressed as follows:

$$\text{FOM} = (1 - T_1)^2 + (0.5 - T_2)^2 + (0.5 - T_3)^2 + (T_4 + T_5 + T_6 + T_7)^2 , \tag{1}$$

where T_1 indicates the passband transmittance at the central frequency f_{goal}, T_2 and T_3 are respectively the transmittances at FWHM ($f_{\text{goal}} \pm B_{\text{FWHM}}/2$), B_{FWHM} is the bandwidth, T_4, T_5, T_6 and T_7 are the transmittances at the frequency points evenly distributed in the off-band.

In order to make the device polarization insensitive, we change the distribution of pixels in the unit structure into 1/8 symmetrical structure, that is, the device is symmetrical not only about the x-axis and y-axis, but also about two diagonals [18]. The unit structure of the THz BPF is shown in Fig. 1(b). Due to the symmetrical structure, only one-eighth of the area needs to be calculated, and the simulation time is greatly reduced.

The parameters of the whole device are set as follows: $f_{\text{goal}} = 0.5$ THz, the period $L = 150/f_{\text{goal}} = 300$ μm. The unit is divided into 20×20 pixels, and the length of the square pixel is $l = L/20 = 15$ μm. The material is aluminum which is also used for device fabrication, having a plasma frequency of 2.24×10^{16} rad/s (or 1.19×10^5 cm^{-1}), a damping coefficient of 1.12×10^{14} rad/s (or 6.47×10^2 cm^{-1}) and a thickness d of 10 μm [19]. These parameters based on the Drude model were input into the FDTD to define the material characteristics. Other relevant parameters in FDTD are set as follows: the simulation duration $t = 200$ picoseconds, the frequency range is 0.1 - 1.5 THz, the global meshing accuracy is 5 μm, and the division accuracy of local mesh is 1 μm.

2.2. BPSO algorithm

DBS algorithm needs to traverse all pixels of the whole device, which is quite time-consuming and easy to fall into the local optimal solution. Therefore, we also use the discrete binary particle swarm optimization (BPSO) algorithm, which is strong in global search ability and directional search [20], to design the THz BPFs.

BPSO algorithm is an evolutionary algorithm to find the optimal solution in discrete space. In BPSO algorithm, the position X and velocity V vectors at a given time i are defined as follows:

$$X(i) = (x_1(i), x_2(i), \cdots, x_n(i)) , \tag{2}$$

$$V(i) = (v_1(i), v_2(i), \cdots, v_n(i)),\tag{3}$$

where each element $x_n(i)$ in the position vector is 0 or 1, and each element $v_n(i)$ is a real number within a specific range. During each iteration, the velocity and position of particles are updated by the following formula [21]:

$$v_{i,d}^{k+1} = \omega^k \cdot v_{i,d}^k + c_1 \cdot r_1 \cdot (p_{i,d}^k - x_{i,d}^k) + c_2 \cdot r_2 \cdot (g_{i,d}^k - x_{i,d}^k),\tag{4}$$

$$x_{i,d}^{k+1} = \begin{cases} 1 & (\text{if } \rho < sigmoid(v_{i,d}^{k+1})) \\ 0 & (\text{otherwise}) \end{cases},\tag{5}$$

$$\omega^k = \frac{(\omega_{ini} - \omega_{end})(K - k)}{K} + \omega_{end},\tag{6}$$

$$sigmoid(v_{i,d}^{k+1}) = \frac{1}{1 + e^{-v_{i,d}^{k+1}}},\tag{7}$$

where ω^k is inertia weight, c_1 and c_2 are the acceleration constants, usually set to 2, r_1, r_2, ρ are random numbers between 0 and 1, $v_{i,d}^k$ and $x_{i,d}^k$ are the velocity and position of the i th particle at a time of k, $p_{i,d}^k$ and g_d^k are the historical best values of a single particle and all particles respectively. K is the maximum number of iterations.

In the design of THz BPFs, we encode the metal or air block as 0 or 1, respectively, and assign them to $X(i)$ in the same order as the DBS algorithm. If the *sigmoid* function is greater than ρ, then $X(i)$ is defined as 1, otherwise it is assigned 0, and then the next calculation is carried out. Five unit structures are randomly generated by BPSO algorithm, and the particle swarm size and the iteration number is set to 5 groups and 65 times, respectively.

3. Simulation results and discussion

We run the two algorithms using a computer with an Intel Core i5-6500 CPU and a 16 G memory. The FDTD settings and objective functions are the same for both algorithms. Figure 2 shows two sets of the optimized unit structures and the transmittance curves obtained by the two algorithms. As shown in Figs. 2(a)–2(d), the final optimized structures of BPSO algorithm and DBS algorithm are totally different, because the FOM function is a group of nonconvex functions, that is, it has multiple local optima, and both of algorithms fall into local optima. DBS algorithm is a local optimization algorithm, which is easy to fall into the local optimal solution, while BPSO algorithm is a global optimization algorithm, which unfortunately falls into the local optimal solution in this work. It may originate from the insufficient size of particle swarm or inappropriate parameter settings, thus the particle swarm converges to the local optimal value. The normalized transmittance curves in Fig. 2(e) and 2(f) for BPSO algorithm has a better out-of-band suppression than those for DBS algorithm in Fig. 2(g) and 2(h), while the transmittances of the corresponding passband peaks are slightly lower.

The variation curves of FOM values in the two algorithms with the number of iteration are shown in Fig. 3. DBS algorithm needs 7 times iterations in total as shown in Fig. 3(a), and a single iteration needs to traverse 55 pixels. Therefore, a total number of 385 FDTD simulations are required for DBS optimization. For BPSO optimization, a total number of 65 iterations are required. A group of particle swarm optimization needs to be calculated for a single iteration for 5 different structures. Therefore, a total number of 325 FDTD simulations are required for BPSO algorithm optimization. The calculation time required for BPSO algorithm to optimize a device is less than that for DBS algorithm. In the comparison, the area, the number of pixels and mesh density in FDTD are set to be the same for both algorithms. The average calculation time of a single simulation is about 30 seconds, so the whole simulation time is about 11550 (385×30) /
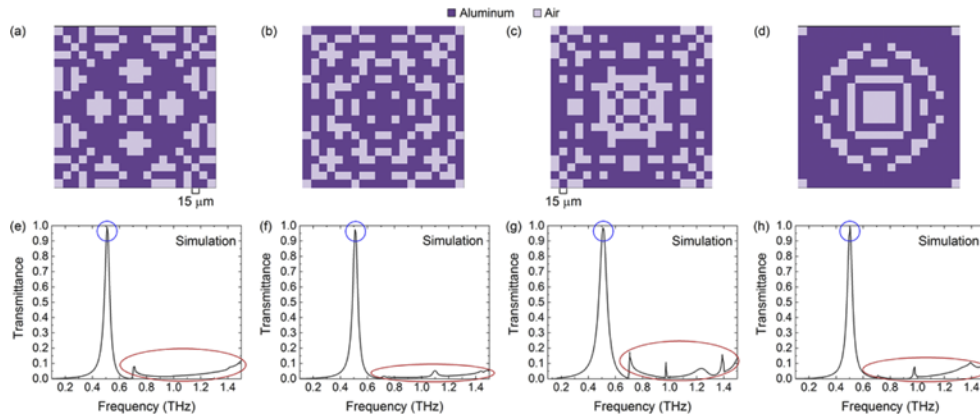
Fig. 2. Comparison of the optimized cell structures and transmittance curves of the THz BPFs obtained by two algorithms. Two optimized structures using the same BPSO algorithm (a-b), and their corresponding transmittance curves (e-f), respectively. Two optimized structures using the DBS algorithm (c-d), and their corresponding transmittance curves (g-h), respectively. Blue and red circles highlight the peak transmittance and out-of-band suppression of the THz BPFs, respectively.
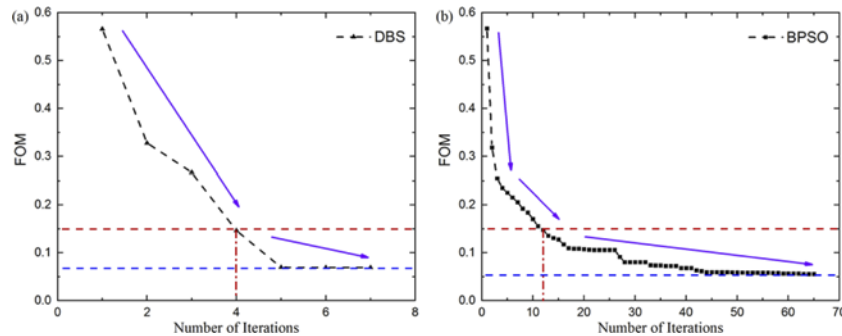
Fig. 3. FOM value versus the number of iteration for two algorithms. (a) DBS algorithm, (b) BPSO algorithm.

9750 (325×30) seconds for DBS/BPSO algorithm, respectively. In practice, we set the iteration numbers of DBS and BPSO algorithms to 7 and 60, respectively.

It can be seen from Fig. 3 that the iterative process of DBS algorithm is relatively gentle, and final FOM value converges to 0.069. The iterative process of BPSO algorithm can be divided into three stages. First stage is indicated by first purple arrow. Due to the large initial value of ω_{ini}, the decline in initial stage is fast. Specifically, for the same FOM value of 0.15, BPSO algorithm only needs 60 simulations, while DBS algorithm needs 220 simulations. When the number of iterations continues to increase, ω^k decreases gradually, and the decline becomes gentle, and finally when ω^k gradually reach to the final value of ω_{end}, FOM value converges pretty slowly and hardly changes, and final FOM value is about 0.056. BPSO algorithm is a global optimization algorithm, and historical/global optimal values will be utilized for the next iteration in optimization process. Therefore, comparing with DBS algorithm, it converges faster in the early stage and the final FOM value is smaller, resulting in a better performance of the BPFs. There are other intelligent algorithms that can be utilized for the reverse design of THz functional devices, including genetic algorithms [22], random hill climbing algorithm [23–24], differential evolution [25–26], artificial bee colony algorithm [26], and swallow swarm algorithm

[27], etc. They may have advantages on designing devices with more complex functions and structures.

4.   Experimental verification

The structure of the device obtained by two algorithms being complicated, it must be simplified to be manufactured according to the processing capabilities of our laboratory. The steps of specific simplification are shown in Fig. 4. Firstly, remove the isolated metal surrounded by air highlighted by red arrows in Fig. 4(a), then approximate the jagged edges with red straight lines shown in Fig. 4(b), and finally remove the rectangles highlighted by red circles on the edges of unit structure in Fig. 4(c), and obtain the simplified structure shown in Fig. 4(d). As shown in Fig. 4(e)-4(h), the transmittance spectra of the filter changes with the simplification of the unit structure. The central frequency of the THz BPF moves from 0.6 THz to 0.82 THz, and the FWHM changes from 0.08 THz to 0.12 THz. It is noteworthy that the peak transmittance is slightly lower and the out-of-band transmittance becomes higher after simplification. After the simplification, the transmittance spectrum is similar to the spectrum of a traditional FSS-based THz filter with cross, Y-shape, or circular apertures [5]. The significant changes of transmittance spectrum indicate that these removed fine features created by the intelligent algorithms deeply affect the bandwidth, transmittance and out-of-band suppression, which adequately reflects the advantages of the RDMs.
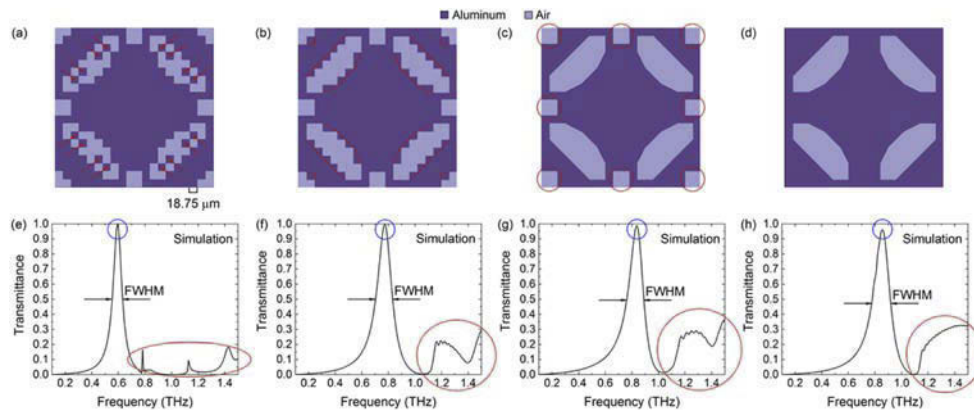

Fig. 4. The process of unit structure simplification (a-d) and the corresponding transmittance spectra (e-h) of a pixel-type THz BPF.

We have prepared a sample on an aluminum foil with a thickness of 10 µm using femtosecond laser micromachining [5]. The sample was characterized by a THz time-domain spectroscopy system, which employed the same femtosecond laser. The femtosecond amplified Ti: sapphire laser (Astrella, Coherent, Inc.) has a wavelength of 800 nm, a pulse width of 35 fs, a repetition rate of 1 KHz, and a pulse energy of 5mJ. The schematic diagrams of the laser micromachining system and the THz system are shown in Fig. 5(a) and Fig. 5(b), respectively. We use pulse energy of 50 µJ, a focusing spot size of 10 µm, and a moving speed 1 mm/second for optimal machining quality. The microscopic image of the sample is shown in Fig. 6(a). The unit structure is consistent with the simplified pattern of the BPF in Fig. 4(d). In the THz system, we used a pair of <110> ZnTe crystals to generate and detect coherent THz radiation with frequency from 0.1 to 2.5 THz through optical rectification and electro-optic sampling, respectively. We used a standard lock-in scheme for time-domain signal detection. In order to eliminate the influence of water vapor absorption on the spectrum, the THz system was fully sealed and filled with dry nitrogen. The sample was placed at the focus of the THz beam with a focal size of about 1.5 mm.
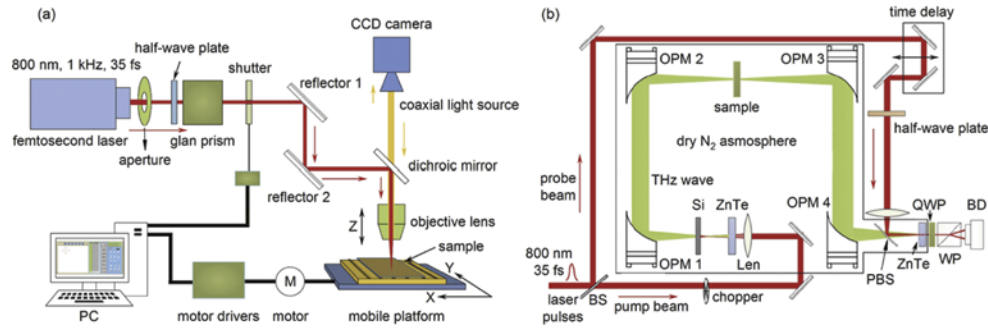
Fig. 5. (a) Schematic diagram of the femtosecond laser micro-machining system; (b) Schematic diagram of the THz time-domain spectroscopy. Legend: BS - beam splitter, OPM - off-axis paraboloidal mirror, QWP - quarter-wave plate, WP - Wollaston prism, BD - balanced detector, PBS - pellicle beam splitter, ZnTe: <110>, 10mm×10mm×1 mm.
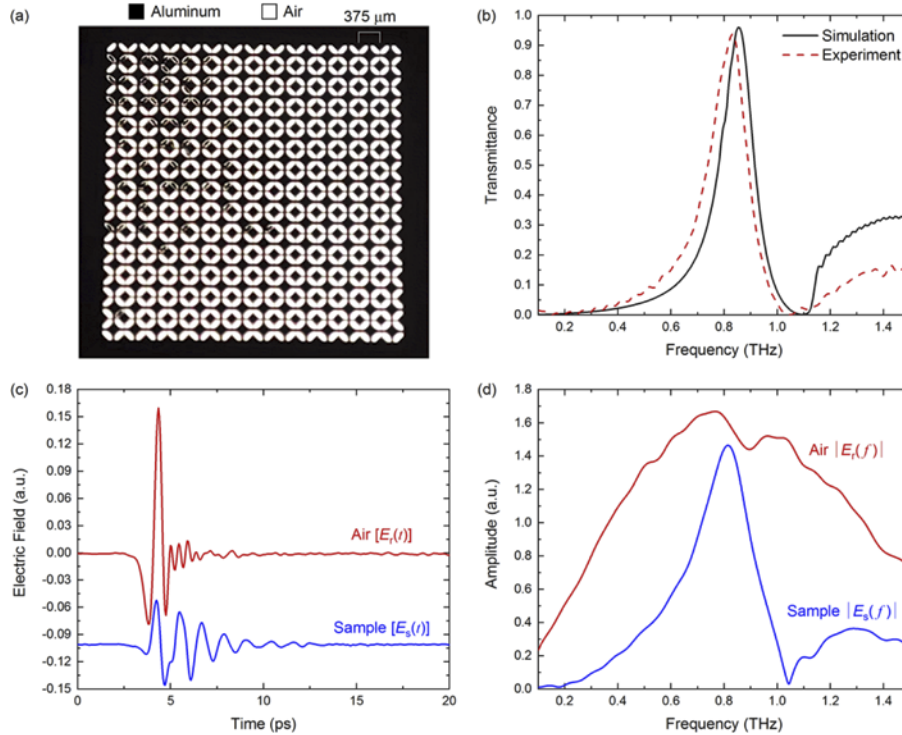
Fig. 6. (a) Microscopic image of a sample fabricated using femtosecond laser micromachining; (b) Transmittance spectra of the sample measured by THz TDS and calculated using FDTD; (c) Time-domain waveforms of the THz pulse through air as reference, $E_r(t)$, and the sample, $E_s(t)$. The two traces are vertically offset for clarify; (d) Frequency-domain THz spectra of the reference and sample.

The measurement results are shown in Fig. 6(b)-6(d), together with the simulation results. The patterned area size in Fig. 6(a) is 5.25×5.25 mm², where black/white area is aluminum/air, respectively. The fabrication quality of the top-left region is not as good as that of other regions due to surface quality of the aluminum foil and repetitive positioning accuracy of the translational stages. It does not affect the performance of the filter much as we can see from the spectroscopy

measurement results shown in Fig. 6(b)-6(d).The calculated frequency range is intentionally set to 0.1 - 1.5 THz to save calculation time. Therefore, we only show the spectra up to 1.5 THz. It can be seen that the experimental results are in good agreement with the simulation results, while the central frequency and peak transmittance are slightly lower than expectations owing to machining errors and imperfect fabrication.

5.   Conclusion

In this work, we construct the inverse design frameworks based on DBS and BPSO algorithms to design pixel-type THz BPFs. It is found that BPSO algorithm converges faster than DBS algorithm because BPSO algorithm is more targeted in each searching direction and can move towards the direction of global optimization. A sample with simplified design was prepared by femtosecond laser micromachining, whose performance characteristics are consistent with FDTD simulation, proving the feasibility of the method. The RDM does not need any known structure or shape. It only needs to specify the design area and iterative parameters to realize the reverse design from specified performance to a target structure.

Disclosures. The authors declare no conflicts of interest.

Data availability. The simulation code/data are available from the corresponding author upon reasonable request.

References

1. Y. S. Lee, *Principles of terahertz science and technology* (Springer, 2009).
2. B. Gao, S. Huang, Z. Ren, Y. Chen, and X. Wang, "Design and verification of an integrated free-standing thick-screen FSS radome," IEEE Antennas Wirel. Propag. Lett. **17**(9), 1630–1634 (2018).
3. E. S. Lee and T. I. Jeon, "Tunable THz notch filter with a single groove inside parallel-plate waveguides," Opt. Express **20**(28), 29605–29612 (2012).
4. S. Savel'ev, A. L. Rakhmanov, and F. Nori, "Using Josephson vortex lattices to control terahertz radiation: tunable transparency and terahertz photonic crystals," Phys. Rev. Lett. **94**(15), 157004 (2005).
5. Y. Lin, H. Yao, X. Ju, Y. Chen, S. Zhong, and X. Wang, "Free-standing double-layer terahertz band-pass filters fabricated by femtosecond laser micro-machining," Opt. Express **25**(21), 25125–25134 (2017).
6. T. Gao, F. Huang, Y. Chen, W. Zhu, X. Ju, and X. Wang, "Resonant Coupling Effects in a Double-Layer THz Bandpass Filter," Appl. Sci. **10**(15), 5030 (2020).
7. F. Hu, Y. Fan, X. Zhang, W. Jiang, Y. Chen, P. Li, X. Yin, and W. Zhang, "Intensity modulation of a terahertz bandpass filter: utilizing image currents induced on MEMS reconfigurable metamaterials," Opt. Lett. **43**(1), 17–20 (2018).
8. X. Ju, Z. Hu, F. Huang, H. Wu, A. Belyanin, J. Kono, and X. Wang, "Tunable ultrasharp terahertz plasma edge in a lightly doped narrow-gap semiconductor," Opt. Express **29**(6), 9261–9268 (2021).
9. G. Zhu, F. Huang, Z. Dai, X. Ju, S. Zhong, and X. Wang, "Reverse design of on-chip terahertz demultiplexers," Micromachines **12**(9), 1093 (2021).
10. Y. Chen, J. Wang, Z. Hu, T. Gao, W. Zhu, and X. Wang, "Fabrication of large-scale freestanding THz wire grid polarizers by femtosecond laser micromachining," Optik **212**, 164655 (2020).
11. J. R. Hu and J. S. Li, "Ultra-compact 1× 8 Channel terahertz Wave Power Splitter," J. Infrared, Millimeter, Terahertz Waves **37**(8), 729–736 (2016).
12. A. Y. Piggott, J. Lu, K. G. Lagoudakis, J. Petykiewicz, T. M. Babinec, and J. Vučković, "Inverse design and demonstration of a compact and broadband on-chip wavelength demultiplexer," Nat. Photonics **9**(6), 374–377 (2015).
13. S. Molesky, Z. Lin, A. Y. Piggott, W. Jin, J. Vucković, and A. W. Rodriguez, "Inverse design in nanophotonics," Nat. Photonics **12**(11), 659–670 (2018).
14. B. Shen, P. Wang, R. Polson, and R. Menon, "An integrated-nanophotonics polarization beam splitter with 2.4 × 2.4 μm² footprint," Nat. Photonics **9**(6), 378–382 (2015).
15. Z. Liu, X. Liu, Z. Xiao, C. Lu, H. Wang, Y. Wu, X. Hu, Y. Liu, H. Zhang, and X. Zhang, "Integrated nanophotonic wavelength router based on an intelligent algorithm," Optica **6**(10), 1367–1373 (2019).
16. J. Huang, J. Yang, D. Chen, W. Bai, J. Han, Z. Zhang, J. Zhang, X. He, Y. Han, and L. Liang, "Implementation of on-chip multi-channel focusing wavelength demultiplexer with regularized digital metamaterials," Nanophotonics **9**(1), 159–166 (2019).
17. H. Kim, I. Park, B.-H. O, S. Park, E. Lee, and S. Lee, "Self-imaging phenomena in multi-mode photonic crystal line-defect waveguides: application to wavelength de-multiplexing," Opt. Express **12**(23), 5625–5633 (2004).
18. A. Fallahi, M. Mishrikey, C. Hafner, and R. Vahldieck, "Efficient procedures for the optimization of frequency selective surfaces," IEEE Trans. Antennas Propag. **56**(5), 1340–1349 (2008).

19. M. A. Ordal, L. L. Long, R. J. Bell, S. E. Bell, R. R. Bell, R. W. Alexander Jr., and C. A. Ward, "Optical properties of the metals Al, Co, Cu, Au, Fe, Pb, Ni, Pd, Pt, Ag, Ti, and W in the infrared and far infrared," Appl. Opt. **22**(7), 1099–1120 (1983).

20. G. Zhu, X. Ju, and W. Zhang, "Multi-objective sequence optimization of PCB component assembly with GA based on the discrete Fréchet distance," Int. J. Prod. Res. **56**(11), 4017–4034 (2018).

21. M. Hajian, A. M. Ranjbar, T. Amraee, and B. Mozafari, "Optimal placement of PMUs to maintain network observability using a modified BPSO algorithm," Int. J. Electr. Power Energy Syst. **33**(1), 28–34 (2011).

22. S. Genovesi, T. Yen, A. Monorchio, E. Prati, Y. Chiang, and F. Costa, "Optimization of wide-bandpass filter within the terahertz frequency regime," in *Proceedings of IEEE Conference on URSI General Assembly and Scientific Symposium* (IEEE, 2011), pp. 1–4.

23. H. Nemat-Abad, E. Zareian-Jahromi, and R. Basiri, "Design of metasurface-based multi-layer THz filters utilizing optimization algorithm with distinct fitness function definitions," Plasmonics **16**(5), 1865–1876 (2021).

24. R. Sharifi, R. Basiri, and E. Zareian-Jahromi, "Optimization-based design of a single-layer wideband reflect array antenna in the terahertz regime," J. Comput. Electron. **19**(1), 469–481 (2020).

25. D. Mandal, R. Kar, and S. Ghoshal, "Digital FIR filter design using fitness based hybrid adaptive differential evolution with particle swarm optimization," Nat. Comput. **13**(1), 55–64 (2014).

26. F. Latifoğlu, "A novel singular spectrum analysis-based multi-objective approach for optimal FIR filter design using artificial bee colony algorithm," Neural. Comput. Appl. **32**(17), 13323–13341 (2020).

27. S. Sarangi, R. Panda, and A. Abraham, "Design of optimal low-pass filter by a new Levy swallow swarm algorithm," Soft Comput. **24**(23), 18113–18128 (2020).